Proceedings of ASME Turbo Expo 2011
GT2011
June 6-10, 2011, Vancouver, British Columbia, Canada

GT2011-46901

STUDY OF UNFORCED AND MODULATED INCLINED FILM-COOLING JETS USING PROPER ORTHOGONAL DECOMPOSITION – PART II: FORCED JETS

Guillaume Bidan **Clementine Vezier** **Dimitris E. Nikitopoulos**

Turbine Innovation and Energy Research (TIER) Center
Mechanical Engineering Department
Louisiana State University,
Baton Rouge, LA, 70803

ABSTRACT

The effects of jet flow-rate modulation were investigated in the case of a 35° inclined jet in cross-flow over a flat plate using Mie scattering visualizations, time-resolved flow rate records and large eddy simulations (LES). In forced experiments, average blowing ratios of 0.3 and 0.4 were investigated with a duty cycle of 50% and pulsing frequencies of St=0.016 and 0.159. Time-resolved flow rate measurements during the experiments provided precise knowledge of the instantaneous jet blowing ratio and adequate inlet boundary conditions for large eddy simulations. The dynamics of the vortical structures generated during the transient parts of the forcing cycle as well as their impact on film cooling performance were investigated with respect of the forcing parameters. At the considered blowing ratios, a starting ring vortex was consistently generated at the transition from low to high blowing ratio. Ingestion of cross-flow fluid at the transition from high to low blowing ratio was also observed and had a negative impact on film cooling performance. All studied cases exhibited an overall decrease in coverage regardless of pulsing parameters over their corresponding steady jet cases at fixed mass flow rate. Comparisons between pulsed and steady jets at constant pressure supply (same high blowing ratio) did exhibit some film-cooling improvement with pulsing. 3D Proper orthogonal decomposition was performed on LES results at distinct forcing frequencies to provide an analysis of dominant modes in the velocity and temperature fields. Significantly different results were obtained depending on the forcing frequency.

NOMENCLATURE

D_j	Jet diameter [*mm*]
L	Jet pipe length [*mm*]
X_j, Y_j, Z_j	Normalized coordinates x/D_j, y/D_j, z/D_j
U, V, W	Velocities along x, y and z axis respectively [ms^{-1}]
T	Temperature [*K*]
BR	Blowing Ratio
BR_m	Mean Blowing Ratio over a cycle
BR_l	Low Blowing Ratio
BR_h	High Blowing Ratio
DC	Duty Cycle [*%*]
f_f	Forcing Frequency [*Hz*]
η	Adiabatic effectiveness $(T_{wall} - T_\infty)/(T_j - T_\infty)$
St	Strouhal number $St = f_f D_j/U_\infty$
t^*	Normalized time $t^* = t\, f_f$
N_r	Number of modes used in POD reconstruction
C_c	Coverage Coefficient $C_c(\eta_x)=1/A_j \int_{\eta\geq\eta_x} dA_{wall}$

Subscripts

j	Jet
∞	Free stream
span	Spanwise averaged quantity
area	Area averaged quantity

INTRODUCTION

Improvement of film cooling systems through geometry optimizations have lead to significant gain in adiabatic effectiveness and decrease in heat transfer coefficients while reducing the sensitivity of those systems to operating conditions variations. However, passive improvements and systems are reaching a point of diminishing returns when subjected to large scale fluctuations of operating conditions such as the one existing beyond the turbine first stage. For strongly varying operating conditions, a more adaptive response through actively controlled film cooling jets appears as a logical step toward more efficient and versatile systems.

Previous studies [1-3] have addressed the effects of cross-flow unsteadiness on film cooling systems and showed that the passive jet flow pulsation due to pressure changes in the cross-flow could have dramatic effect on film cooling performance.

To alleviate these effects, [2, 4-5] have studied the potential of fully modulated film cooling jets without reaching a consensus on the actual success of such solution. A more detailed literature review can be found in Part I [6] of this two-part paper. The current work aims at answering some of the questions associated with forced film cooling jets by carefully considering the physics involved with those systems and their impact on film cooling metrics by mean of experimental visualizations and Large Eddy Simulations. In addition, 3D Proper Orthogonal Decomposition (3D-POD) is performed on selected simulation results to provide a modal analysis of both temperature and velocity fields. This constitutes the first step towards obtaining of a reduced order model for film cooling jets, necessary to the development of a controller toward improved performance.

In Part I [6] of this study, the unforced jet was extensively investigated and compared to similar results previously obtained with a vertical jet setup from [7]. The characteristic vortical structures of the attached jet (BR<0.4) and detached jet (BR≥1.0) regimes, as well as the transition from one to the other, were documented using reactive Mie scattering and Large Eddy Simulations. Adiabatic effectiveness trends were obtained and compared to comparable vertical jet results. Three dimensional proper orthogonal decomposition (3D-POD) was carried out on the LES velocity and temperature fields at BR=0.15. The most energetic POD modes were associated to shear layer hairpin vortices and carried almost 30% of the total kinetic energy, while higher order modes appeared to be correlated to less energetic wall structures.

Part II of this work investigates the same system under forced conditions. First, the characteristic vortical structures due to jet forcing will be described, followed by a comparison of the forced jet film cooling performance with unforced results presented in PartI [6]. Finally, 3D-POD will be applied to two sets of LES results at distinct forcing frequencies.

EXPERIMENTAL AND NUMERICAL SETUP

Experiments were conducted in an open loop wind tunnel schematically shown in Fig. 1 with a single jet mounted flush to the bottom wall at an angle of 35° with respect to the cross flow direction and no compound angle. Additional details for the experimental setup are provided in Part I [6].

The jet supply system consisted of two branches, one principal and one bypass, each comporting a metering needle valve to control the flow in the branch. The bypass also comported a computer-controlled solenoid valve which was used to pulse the flow (Fig. 1). This system gave the ability to set independently low and high flow rates, hence setting the corresponding blowing ratios, BR_l and BR_h, in forced experiments while the valve opening time set the duty cycle (DC). An inline flow-meter was used to record instantaneous flow-rates. Laser–sheet, Mie-scattering visualizations (both fully reacted and reactive), and time resolved flow-rate measurements were handled through A/D converters and a control system allowing synchronized acquisition and actuation.

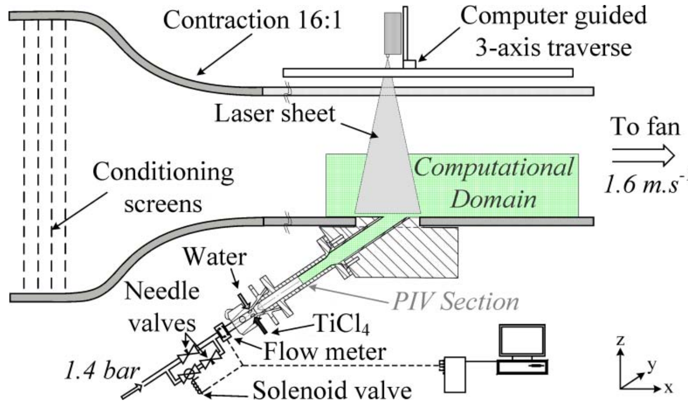

Figure 1 – Experimental setup.

The experiment was designed so that the jet natural frequencies were relatively low (<100Hz) and forcing was applied at frequencies lower than these natural frequencies consistently with the scaled-down (relative to this work) experiments of [4] and theoretical assessments of [8].

Numerical Large Eddy Simulations (LES) were carried out paralleling the experiments using Fluent™ to provide additional information on the vortical structures and velocity field. Velocity boundary conditions for the cross-flow were provided from experimental hotwire measurements while at the inlet of the jet pipe a uniform velocity profile was modulated by using the signal of the unsteady volumetric flow rate measurement from the flow-meters during experiments. The jet and cross flow fluids were maintained at constant temperature of respectively 300 and 330K, which did not affect the velocity field. Further details about the numerical simulations are provided in Part I [6].

PULSED JET

Forced jet experiments were carried out using a nominal square wave excitation according to the forcing parameters summarized in Table 2. Both of those cases have been observed at 4 forcing frequencies of 0.5, 1.0, 5.0 and 10.0Hz, respectively corresponding to Strouhal numbers of St=0.008, 0.016, 0.079 and 0.159.

Table 1 – Forcing conditions

Case	BR_l	BR_h	BR_m	DC
I	0.150	0.450	0.30	50
II	0.150	0.750	0.40	50

Jet Regimes

The use of time-resolved flow-meter measurements allowed for precise verification of the forcing conditions. Typical phase-averaged flow meter records are provided in Fig. 2a and 2b respectively corresponding to Case I at St=0.016 and 0.159. In the time records, flow-rate oscillations are observed at the transition from the low part to the high part of the cycle and inversely. These correspond to an acoustic resonance consistent with Helmholtz volumetric modes attached to the system dimensions at a constant frequency of St=0.8 throughout the tests and regardless of forcing parameters. Such modes are commonly found in forced systems and present in numerous studies such as [9] or [10].

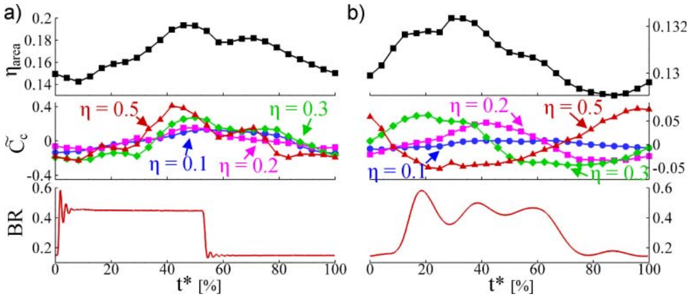

Figure 2 – Phase Averaged η_{area} (*top*), relative coverage coefficient fluctuation for η=0.1, 0.2, 0.3 and 0.5 (*center*), blowing ratio (*bottom*) for Case I at a) St=0.016; b) St=0.159.

At the transition from BR_l to BR_h, the sudden rise in flow-rate results in increased shear at the jet/cross-flow upstream interface, triggering the rolling of the upper shear layer to form a starting vortex, visible in Fig. 3a corresponding to Case I at St=0.016. Conversely to the vertical jet of [7], no rollup is clearly observed in the lower shear layer, suggesting the starting vortices in the inclined jet configuration at low blowing ratio are of the inverted (negative) hairpin type rather than (positive) hairpin or ring vortices. It should be noted that in Fig. 3b, three individual structures are observed corresponding to three distinct rollups of the jet shear layer. It is unsure if the multiplicity of starting structures should be attributed to the blowing ratio oscillations of Fig. 2 or to the formation of wake structures usually observed in the vertical jet configuration at stroke ratios above the formation number (see [7]). In Fig. 3b as the starting vortices penetrate in the free stream, secondary starting hairpin vortices develop directly downstream of them due to the induced gradients in vertical velocity and from the natural shear with the crossflow. Eventually, the primary starting vortices are diffused by the overall positive vorticity and only the secondary starting vortices remain as shown in Fig. 3c. The transient behavior induced by the change in blowing ratio is ultimately washed out and the jet behaves in a quasi-steady manner as seen in Fig. 3d. The impact of the starting structures on the temperature field was studied using LES results of Case I and II at St=0.016. Figure 3 attests to the qualitatively good agreement between LES results and experimental observations. In Fig. 4 instantaneous wall adiabatic effectiveness and Laplacian of the pressure iso-surfaces are presented. For Case I in Fig. 4b-d, an increase in spread around the jet exit is observed at the onset of the high blowing ratio due to jet fluid exiting on the side of the jet exit. The coverage is also affected by the velocity field induced by the secondary starting vortices and the associated crossflow fluid entrainment. A 'pinch' in the coverage develops near the secondary starting structures legs as they are convected downstream. In Fig. 4e, the jet behaves in a quasi-steady manner. For Case II corresponding to a higher value of BR_h, although a mild increase in the spread can be found in Fig. 4j-l, the cooling performance of the jet is significantly degraded as the jet lifts partially off the wall immediately after the transition to BR_h.

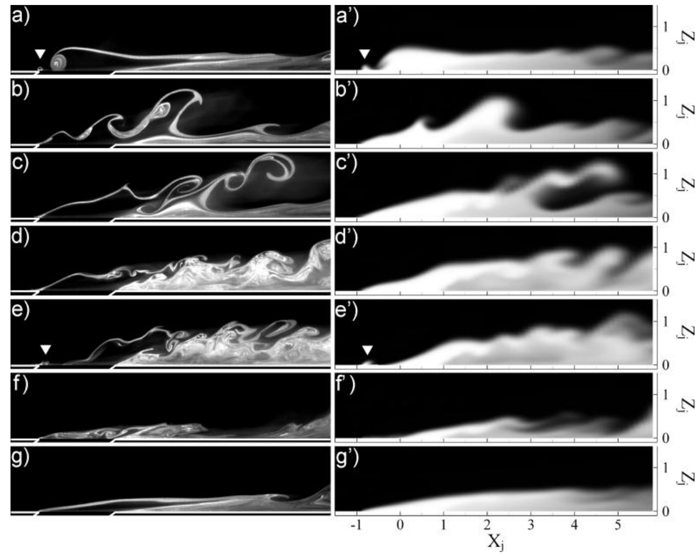

Figure 3 – Instantaneous reactive Mie scattering visualizations in the plane Y_j=0 (*left*) and temperature field from LES (*right*) at a) t*=4; b) t*=9; c) t*=13; d) t*=53;e) t*=57; f) t*=69; g) t*=97 for Case I at St=0.016.

At the transition from BR_h to BR_l, the rapid decrease in flow rate is accompanied by a pressure wave traveling inside the jet pipe, resulting in an ingestion of cross-flow fluid at the jet inlet observed in both experiments in Fig. 3e and simulations in Fig. 3e'. In Fig. 5 the temperature fields for both Case I and II at St=0.016 are shown at t*=56% (30ms after the transition from BR_h to BR_l). In both cases the flow separates inside the jet pipe and crossflow fluid is ingested at the upstream edge of the jet while the horseshoe vortex formed during the high part of the cycle is convected downstream (see Fig. 4f and 4m). The ingestion is more consequent in Case II with greater BR_h as the mass deficit at the closing of the solenoid valve is greater. Although the ingestion causes a disturbance and a disruption of coolant supply for short amount of time it will significantly affect the coverage during most of the low part of the cycle. Indeed in Fig. 3f and 3f' even 140ms (t*=69%) after the transition from BR_h to BR_l, the jet has not recovered from the ingestion and a clear coverage breakup is visible around X_j=4. In Fig. 4f-g for Case I (BR_h=0.45), the effect of the ingestion is visible mainly in the near-field of the jet exit while in Fig. 4h, 435ms (t*=97%) after the transition, the values of adiabatic effectiveness and the spread beyond X_j=7 are still low compared to the one immediately before the jet onset (Fig. 4a) or the corresponding steady state at BR=0.15 (see PartI [6]). Figure 4m-p shows results for Case II (BR_h=0.75) after the valve closing where coverage breakup is even more significant when comparing with Case I at identical phase positions. While the wall coverage is still redeveloping when the next pulse is triggered, vortical structures formed in the jet shear layers are of the hairpin type and consistent with the corresponding steady state jet at BR=0.15.

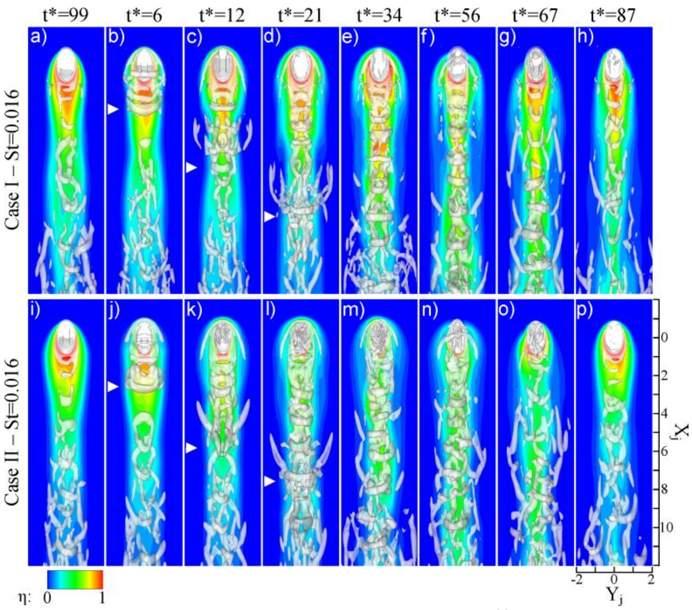

Figure 4 – Instantaneous wall adiabatic effectiveness and Laplacian of the pressure iso-surfaces from LES for Case I (*top*) and Case II (*bottom*) at St=0.016 at t*=99, 6, 12, 21, 34, 56, 67 and 87%.

Case I and II were also investigated at lower (St=0.008) and higher forcing frequencies (St=0.08, 0.159). At St=0.008 the jet behavior was sensibly identical to the previously presented cases at St=0.016 with two transient phases and two quasi-steady regimes. However, cases at St=0.08 and St=0.159 had cycle periods short enough to prevent the jet settling in both high and low part of the cycle so that no quasi-steady regime was observed. Figure 6 shows a series of reactive Mie scattering visualizations corresponding to Case I at St=0.08. In Fig. 6a and 6b the starting vortices of the current cycle can be seen forming above the jet exit in a similar way as the one observed at St=0.016, along with the remnants of the secondary starting vortices from the previous cycle (pointed at by an arrow). In Fig. 6c the valve is closed almost immediately after the formation of the starting structures so that the jet does not settle into a quasi-steady regime. Crossflow ingestion occurs at the jet upstream edge in Fig. 6c (tailless arrow) and still affects the flow in Fig. 6d shortly before the next pulse.

Figure 7 shows similar views as those presented in Fig. 4 from simulations at St=0.159. Instantaneous coverage is brought to the wall essentially by the secondary starting vortices (tailless arrows) as they are convected downstream which are the dominant vortical structures formed during the cycle. In Fig. 7a-d for Case I (BR_h=0.45), the coverage beyond X_j=6 is marginal as the starting structures consistently lift off the wall at this level. In Case II (BR_h=0.75) with a higher value of BR_h, the average coverage breakup point is even closer to the jet exit, about X_j=4, as the starting structures posses more strength and vertical momentum compared to the previous case, thus lifting off earlier. In both cases, large 'X' patterned structures, from the combination of two side vortices, are formed ahead of the starting structures and while the upper legs of the 'X' appear to affect negatively the coverage as the velocity field they generate near the wall is oriented toward the symmetry plane, the lower legs of the 'X' with opposite vorticity tend to favor the spread, hence the 'rosary' like pattern observed at the wall from the succession of pinch/spread.

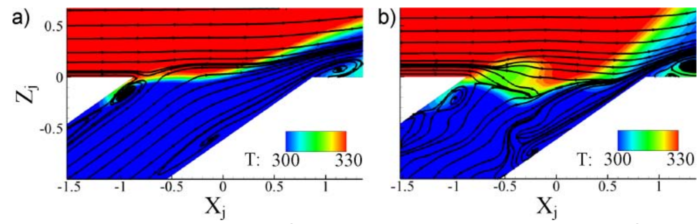

Figure 5 – Temperature field and 2D U-W streamlines for a) Case I; b) Case II at t*=56%.

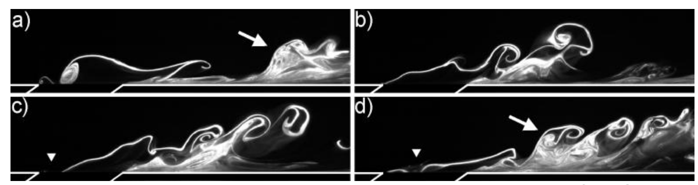

Figure 6 – Reactive Mie scattering visualizations for Case I at St=0.08 at a) t*=13%; b) t*=43%; c) t*=60%; d) t*=90%.

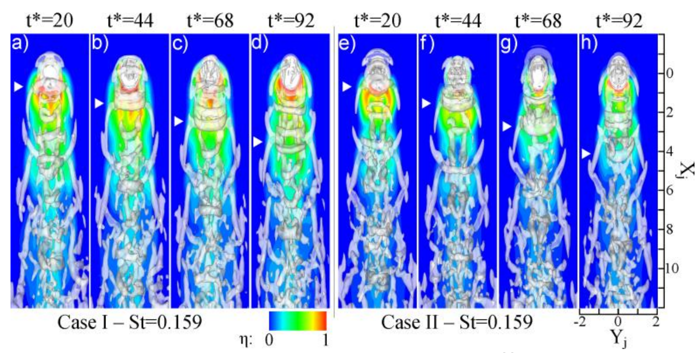

Figure 7 – Instantaneous wall adiabatic effectiveness and Laplacian of the pressure iso-surfaces from LES for Case I (*left*) and Case II (*right*) at St=0.159 during a forcing cycle.

Film Cooling Performance

As for the steady jet, quantitative information was extracted from the LES simulations to assess the instantaneous as well as average performance of the forced jet. Figure 8 presents time averaged η_{span} and $\eta_{centerline}$ values for Case I and II along with relevant steady state trends at constant low, high and average blowing ratios. For Case I, the span-wise average effectiveness trends (Fig. 8a) show that the forced cases at St=0.016 and St=0.079 have performance comparable to the case at BR=BR_h=0.45 with yet an average mass-flow rate 1.5 times lower. These observations are consistent with the findings of [4]. On the other hand, the centerline adiabatic effectiveness (Fig. 8b) appears to be greatly affected by jet forcing and decreases consistently with increasing forcing frequency. The

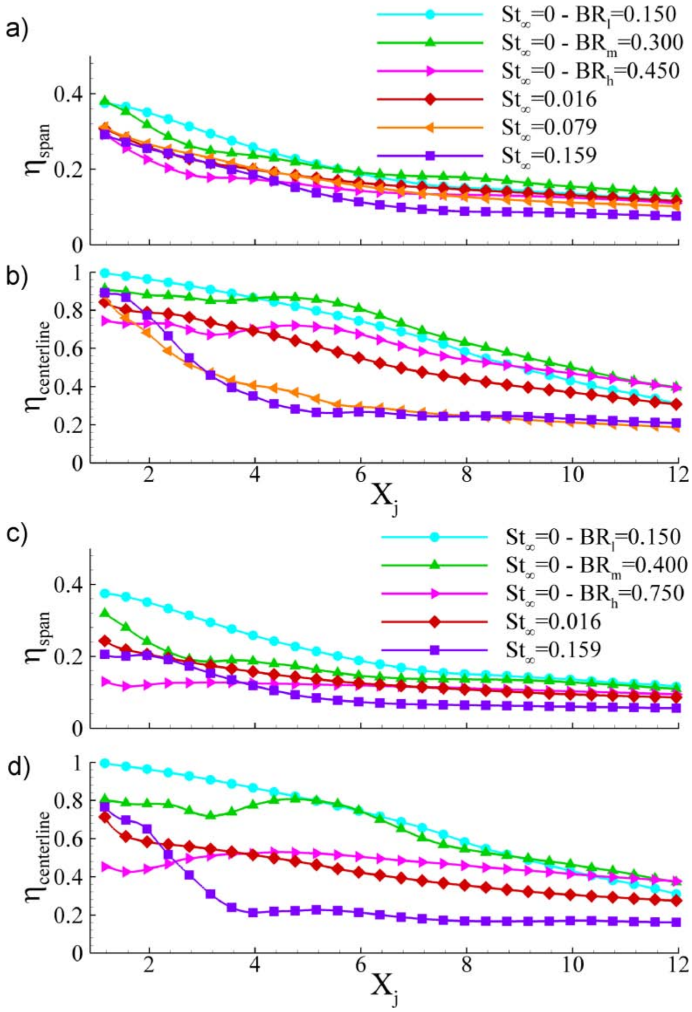

Figure 8 – Spanwise averaged Center line (*top*) and (*bottom*) adiabatic effectiveness from LES for the forced inclined jet for a, b) Case I; c, d) Case II.

case at St=0.016 still shows reasonable centerline performance, though inferior to the compared steady state values while the two trends at St=0.079 and St=0.159 reveal overall degraded $\eta_{centerline}$ values. Directly downstream of the jet exit the case at St=0.159 shows improvement over the other forced cases and the steady state at $BR=BR_h=0.45$. For η_{span} as for $\eta_{centerline}$, increases in forcing frequencies have a negative impact on the jet performance. The combination of both $\eta_{centerline}$ and η_{span} suggests an increase in spread for the forced cases with overall more homogeneous wall adiabatic effectiveness values over the steady state. In Fig. 8c for Case II, although no improvement in η_{span} is found in forced cases over the $BR=BR_l$ and $BR=BR_m$ steady state cases, forcing the jet at St=0.016 provided overall higher η_{span} values than the one at $BR=BR_h$ particularly for $X_j<6$. At St=0.159 higher η_{span} values were achieved for $X_j<4$ over the case at $BR=BR_h$ with lower values downstream of this point. Concerning the centerline adiabatic effectiveness in Fig. 8d, no improvements are observed in forced conditions over the unforced cases at $BR=BR_l$ and $BR=BR_m$ but higher $\eta_{centerline}$ values are achieved over the case $BR=BR_h$ for St=0.016 and St=0.159 for respectively $X_j<4$ and $X_j<2.5$.

The phase averaged temporal evolutions of the coverage were established for Case I at St=0.016 and St=0.159 and are shown respectively in Fig. 2a and 2b. In these figures a certain delay between the values of η_{area} with respect to the instantaneous blowing ratio is expected as the wall values do not respond immediately to events occurring at the jet exit since the flow is mostly dominated by convective phenomena. The lower forcing frequency case clearly shows the negative impact of the transition from BR_h to BR_l on the value of η_{area} due to the ingestion of crossflow fluid at the jet exit and the momentary disruption of coolant. As mentioned previously while commenting Fig. 4, even though this event occurs at t*≈50%, the coverage is degraded all along the low part of the cycle and increases again only after the onset of the high part of the following cycle. A stall in the progression of the coverage during the high part of the cycle is observed around t*=45% as the jet enters the quasi-steady regime mentioned earlier. The amplitude of the variations during a cycle is significant when compared to the steady state values (see PartI [6], Fig. 10a**)**. The averaged maximum η_{area} value over a cycle reaches 0.193 (with instantaneous peaks at above 0.20) which is virtually identical to the maximum value encountered in steady state at BR=0.3 (η_{area}= 0.196). The relative variations of the coverage coefficients ($\widetilde{C_c} = (C_c - \overline{C_c})/\overline{C_c}$) are provided in Fig. 2a. The evolution of the coverage coefficient during the cycle is similar to the evolution of η_{area} with decrease in the low part of the cycle and increase in the high part. The trends of the coverage coefficient for the higher values of η respond faster to the changes in blowing ratio since the regions of higher effectiveness are usually closer to the jet exit. Jet forcing introduces greater relative variation of the coverage coefficient related to higher values of the adiabatic effectiveness. Indeed, while $C_c(\eta=0.1)$ has a relative standard deviation of 9% over a cycle, the same quantity increases to 20% for $C_c(\eta=0.5)$ and 28% for $C_c(\eta=0.75)$. Although the effects of each transient regime were observable in the forced case at St=0.016, the short time scales involved at St=0.159 make this impossible since multiple cycles effectively impact the instantaneous wall temperature field, hence the phase shifts in the variations of C_c at different threshold η. Overall the coverage appears relatively constant over a cycle and the relative standard deviation for η_{area} is only 0.9% (compared to 9% at St=0.016) and the relative standard deviation for $C_c(\eta=0.1)$ and $C_c(\eta=0.5)$ are respectively 0.6% and 4.5%.

POD Analysis

As for the steady state, LES flow fields and temperature fields for Case I at St=0.016 were analyzed using 3D-POD. The domain and spatial sampling used for the forced cases were identical to the one described in PartI [6]. Based on the work of [11] on 2D-POD of a pulsed detached jet in cross-flow, the an initial temporal sampling of 25 phase locked positions over 10 periods was investigated. However, given that the forcing signal used in [11] was a sinusoidal, thus significantly different

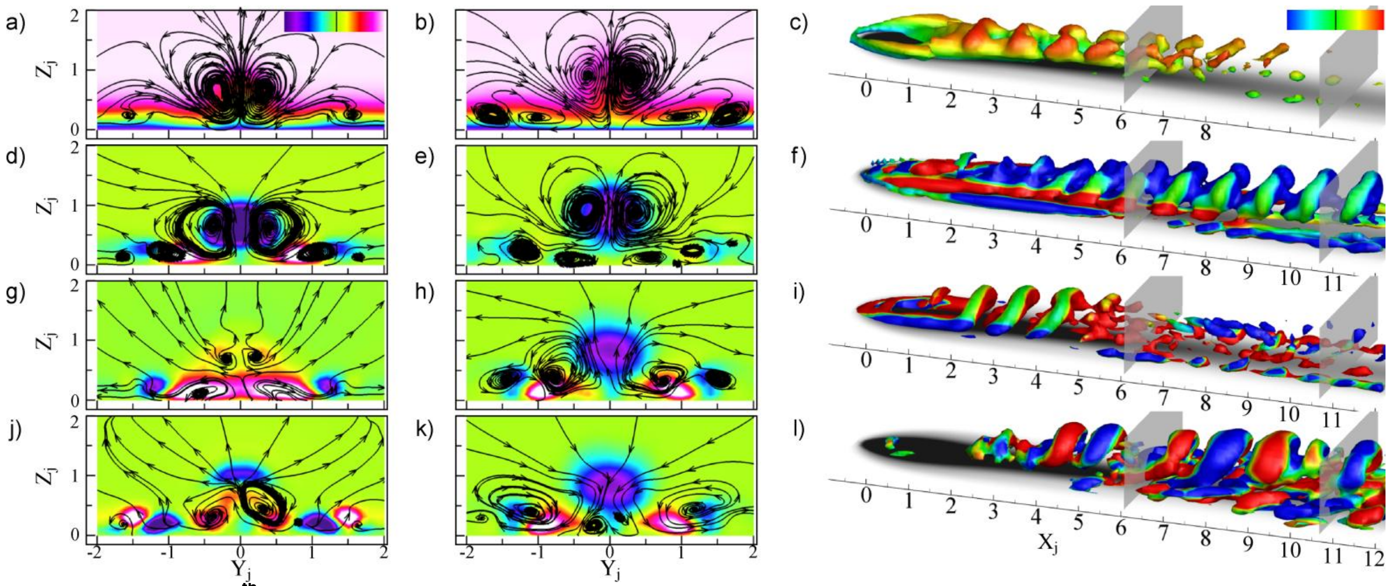

Figure 9 – Mean flow (0th POD Mode) and first significant velocity POD modes for Case I at St=0.016 a-d) Mode0; e-h) Mode1; i-l) Mode2; m-p) Mode6. Slices at X_j=6 (*left*), X_j=10.6 (*right*) with U-velocity contours and V-W streamlines. Q-Criterion iso-surfaces (*right*) from corresponding POD modes colored by U-velocity and mean wall temperature contours (*grey scale*).

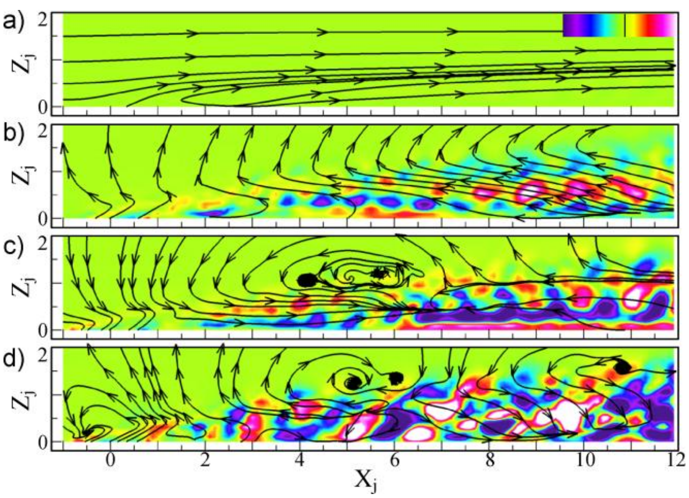

Figure 10 – Mean flow and first significant velocity POD modes for Case I at St=0.016; a-d) Mode0; e-h) Mode1; i-l) Mode2; m-p) Mode6. Slices at Y_j=0 with V-velocity contours and U-W streamlines.

from the square wave used in the current study, a finer sampling of 50 phase locked positions over 10 cycles was preferred. The POD was computed on both the full time sequence and the phase averaged signal. As seen in Fig. 12, both methods provided sensibly similar results for the first 20 modes and started to diverge for higher order modes. This result is expected and consistent with the findings of [11]. Indeed, when considering the complete time sequence, the fluctuation part due to more fine-grained turbulence is included in the signal and requires a large number of modes to be fully resolved. On the other hand, when analyzing the phase averaged signal, the turbulent fluctuation is removed from the signal thus requiring fewer modes to capture the bulk flow fluctuations (phase

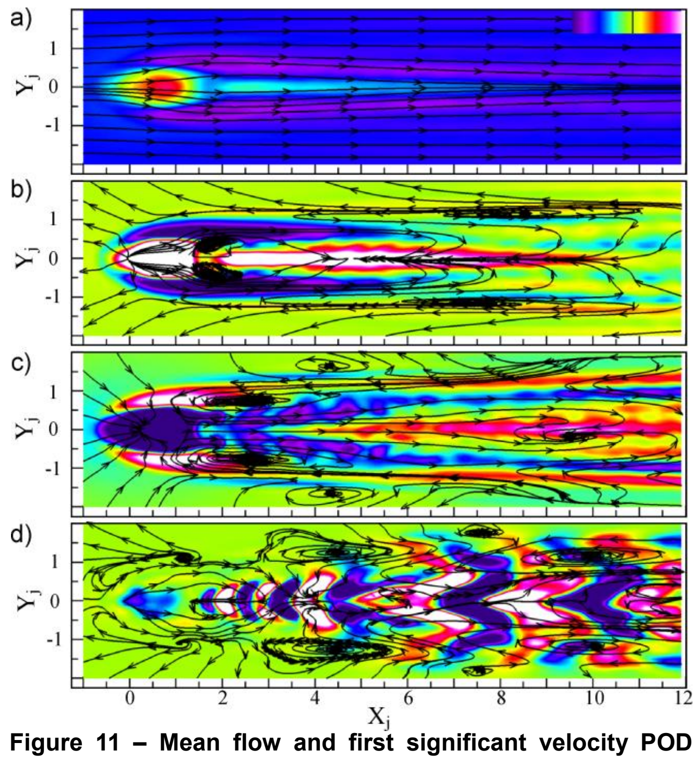

Figure 11 – Mean flow and first significant velocity POD modes for Case I at St=0.016; a-d) Mode0; e-h) Mode1; i-l) Mode2; m-p) Mode6. Slices at Z_j=0.25 with W-velocity contours and U-V streamlines.

averaged). While in the steady state POD analysis, the turbulent fluctuations were considered important to model the flow behavior, in the pulsed system, the significant part was considered to be the phase averaged variation thus the results presented in this paper are based on the POD analysis of the phase averaged signal.

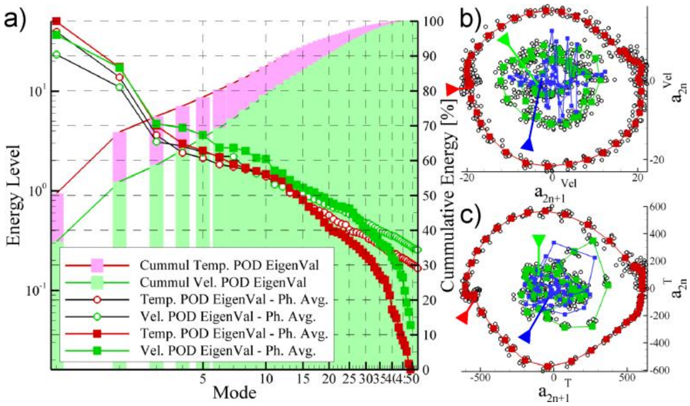

Figure 12 – POD decomposition metrics for Case I at St=0.016 a) Temperature and velocity POD modes eigen values and cummulative energy; b) Velocity POD coefficients; c) Temperature POD coefficients. Open symbols correspond to full time sequence POD. Arrow points toward t*=0 in the time sequence.

For the sake of brevity, Fig. 9, 10 and 11 only present modes 0, 1, 2 and 6 issued from the decomposition of Case I at St=0.016. As for the steady state, the 0^{th} mode corresponds to the average flow field. Based on the interpretations of the velocity field corresponding to each mode it is possible to qualitatively identify which features of the forced jet are being captured by individual modes. The 1^{st} mode corresponds to the bulk flow fluctuation associated with the change in blowing ratio and captures the global jet expansion and shrinking occurring during a cycle. No evidence of a vortical structure is observed in the upper shear layer in Fig. 10b, although a counter rotating vortex pair is visible in the constant X_j slices of Fig. 9d and 9e. The 2^{nd} mode exhibits large scale structures in the jet upper shear layer in Fig. 10c, converging velocity field toward the jet exit as well as strong vertical vorticity in the plane Z_j=0.25 of Fig. 11c, and is predominantly significant in the near field of the jet in Fig. 9i. These considerations suggest that Mode2 is correlated to the large scale structures introduced at the transition from BR_l to BR_h and from BR_h to BR_l, i.e. starting vortices and ingestion. It should be noted that in this forced case, the cumulative captured kinetic energy of modes 1 and 2 is equivalent to 53% of the total kinetic energy which is to be put in perspective with the 30% in the steady state case at BR=0.15. Modes 3 to 5 appear similar to the 2^{nd} mode yet with finer scales but were predominant in the near field of the jet exit. They were considered as dominated by smaller scale perturbations associated with the introduction of the transient regimes and thus were not presented here for brevity. Mode6 however shows in Fig. 10d the presence of shear layer vortices consistent with the natural hairpin vortices encountered in unforced conditions, and the Q criterion iso-surfaces of Fig. 9m are similar to the one found in dominants modes at BR=0.15 (see PartI [6]). This implies that the 6^{th} mode is related to the quasi-steady behavior during either the low or high part of the cycle. This last point will be developed later and lead to the observation of the POD mode segregation.

Conversely to the steady state, the circular shape of the phase diagram in Fig. 12b should not be interpreted as a sign of correlation between the 1^{st} and 2^{nd} modes since the signal is by nature periodic. However, the circular shape shows that both modes operate at the same frequency and with almost equal influence. Interestingly, clusters of points can be observed before the beginning (red arrow) of the cycle and before the transition from high to low blowing ratio (diametrically opposed to the red arrow) where both 1^{st} and 2^{nd} mode values stagnate, the former at a maximum (or minimum) and the latter at a zero value. This observation confirms the qualitative interpretation previously made where Mode1 would correspond to the bulk modulation of the jet envelope thus would be predominant away from the transition points, and Mode2 would correspond to the large scale structures of the transition and would have high values at the transitions.

The temperature field was analyzed as well using POD, the results of which are presented in Fig. 13, 14 and 15. At this point it should be reminded that while the POD has an optimal character when dealing with velocity field since it maximizes the kinetic energy, the natural norm associated with it does not maximize thermal energy, thus the temperature decomposition cannot be considered as optimal. Such discussion is carried out in further details in PartI [6]. Similarly to the velocity field decomposition, the 0^{th} mode in Fig. 13a-c, 14a and 15a corresponds to the average temperature field, while Modes 1 and higher correspond to the fluctuations around this time averaged field. As for the velocity decomposition, the 1^{st} mode, which is the most "energetic", appears to describe the global temperature fluctuations due to the change in penetration associated with jet forcing. The 2^{nd} mode shows a more localized distribution with positive values in the vicinity of the jet exit and negative values in the far field. The phase diagram in Fig. 12b shows similarities with the one of the velocity field and suggests that while Modes1 and 2 have similar overall impact in terms of amplitude and frequency, the moments at which they are acting on the flow are different. Hence Mode1 has a stronger influence away from the transitions while Mode2 affects the flow mainly at the transitions moments. Modes 3 to 9 exhibited distributions similar to the one of Mode2 with yet smaller length scales and were considered to describe the smaller scale perturbations introduced by the transients thus not presented here. The 10^{th} mode though shows fluctuations in the jet shear layer further away from the jet exit which are consistent with the one observed in unforced conditions at BR=0.15 (see PartI [6]) and suggest this mode captures the quasi-steady nature of the jet away from the transitions.

To confirm the qualitative interpretations of the POD modes the coefficients a_1, a_2, a_6 for the velocity field and a_1, a_2, a_{10} for the temperature were plotted in Fig. 16a versus t* along with the phase averaged blowing ratio profile. For both velocity and temperature decompositions, a_1 has broad periods of maxima in absolute value beyond t*=20% up to t*=55% and from t*=80% to t*=100%, both corresponding to the respective established quasi-steady state regimes while a_2 exhibits more localized

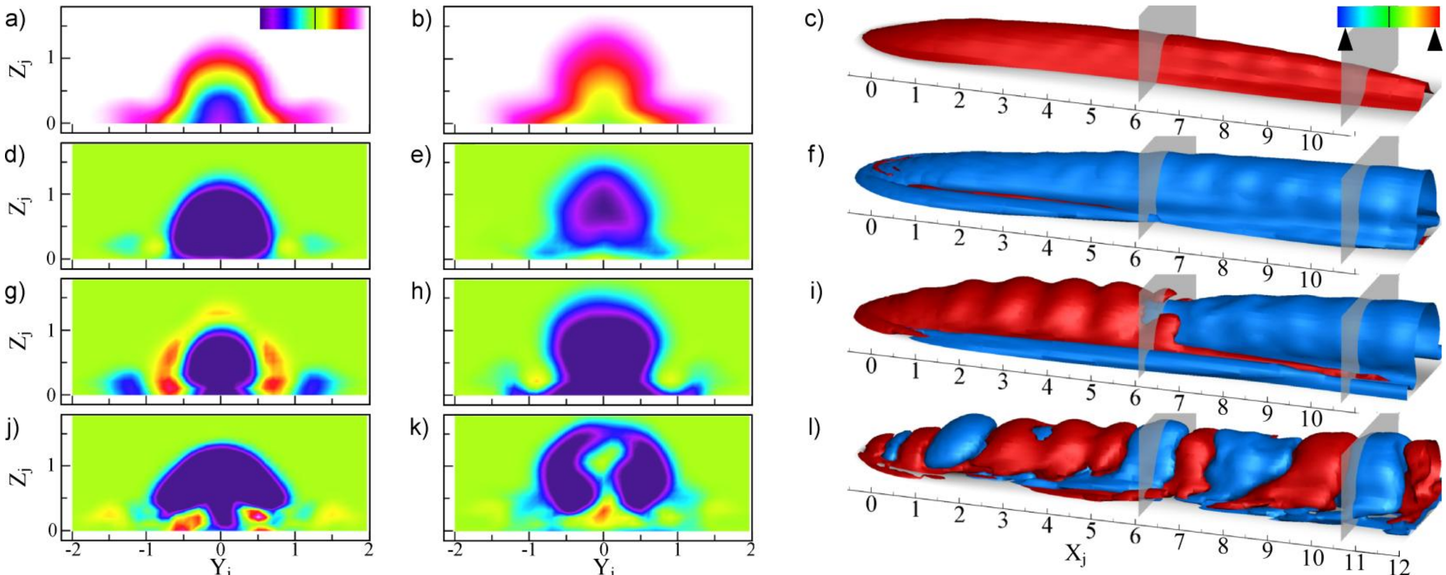

Figure 13 – Mean temperature field (0^{th} POD mode) and first significant temperature POD modes for Case I at St=0.016 a-d) Mode0; e-h) Mode1; i-l) Mode2; m-p) Mode10. Slices at X_j=6 (*left*), X_j=10.6 (*center*) with temperature contours. Iso-temperature surfaces (*right*) computed from the corresponding POD modes and mean wall temperature contours (*grey scale*).

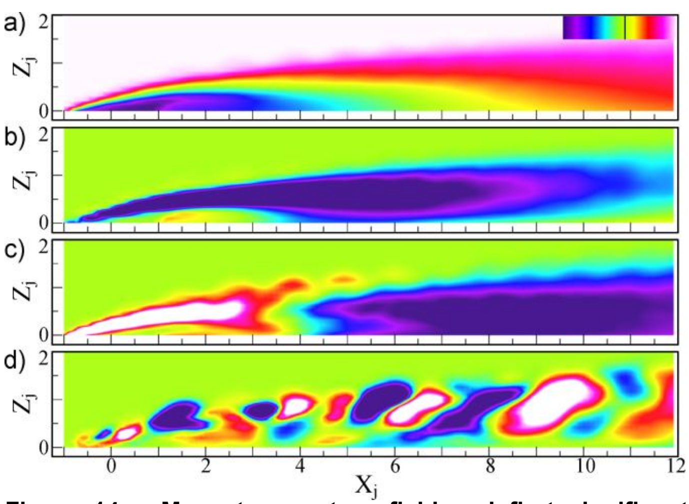

Figure 14 – Mean temperature field and first significant temperature POD modes for Case I at St=0.016 from LES; a-d) Mode0; e-h) Mode1; i-l) Mode2; m-p) Mode10. Slices at Y_j=0 with temperature contours.

maxima, directly after the transitions, from one part of the cycle to the other. Modes 6 for velocity and 10 for temperature have significant values during the quasi-steady state period in the high part of the cycle also confirming the qualitative analysis. The plots of intermediate coefficients (a_3 to a_5 for velocity and a_3 to a_9 for temperature) showed that their support of action was also localized within the transient regions of the cycle and the amplitude of their respective maxima was decreasing along with the width of the peak, traducing a more localized and finer scale influence. Although the transient and the high quasi-steady regimes appeared to be captured by modes 1 to 6, none of the first significant modes, except for the first one describing the bulk flow modulations, had significant non-zero values during the low quasi-steady part of the cycle. Only beyond the

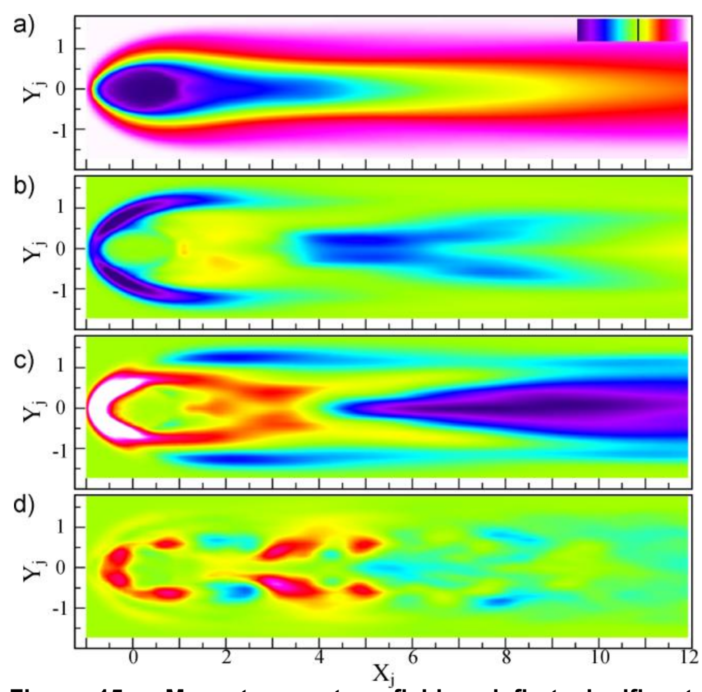

Figure 15 – Mean temperature field and first significant temperature POD modes for Case I at St=0.016 from LES; a-d) Mode0; e-h) Mode1; i-l) Mode2; m-p) Mode10. Slices at Z_j=0 with temperature contours.

40^{th} mode would the support of action be localized during this part of the cycle as seen in Fig 16a for a_{41} (multiplied by 10 to increase visibility). This can be explained by the fact that vortical structures formed during the low quasi-steady part of the cycle are relatively weak in terms of energy, compared to the transient vortical structures or even the one formed during the quasi-steady high part of the cycle, thus are relegated to the end of the POD spectrum as weak perturbations.

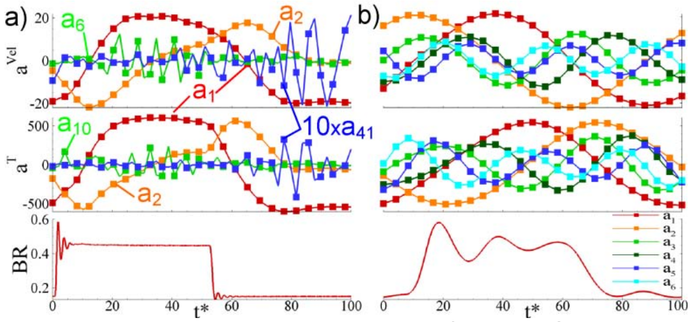

Figure 16 – Temporal evolution of the POD modes coefficients a_i for the velocity (*top*) and temperature (*middle*) decompositions along with forcing blowing ratio profile (*bottom*) at a)St=0.016; b)St=0159.

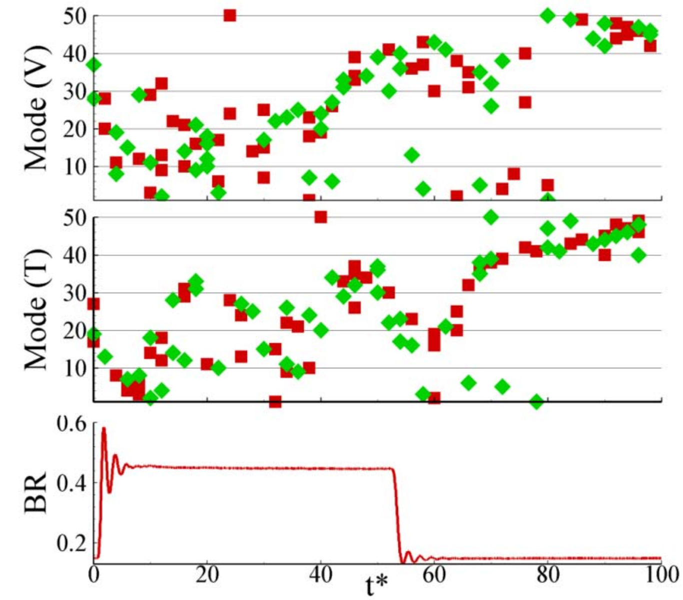

Figure 17 – Phase distribution of the minima (*green diamond*) and maxima (*red squares*) associated with the POD modes coefficients a_i for the velocity (*top*) and temperature (*middle*) along with forcing signal (*bottom*).

Figure 17 shows the phase locations of the maximum and minimum values of the modal coefficients for each mode revealing the moment in the cycle where they have maximum influence. For both velocity and temperature, a clear pattern appears in the distribution of the maxima and minima. Indeed most of the 40 first modes appear to have an influence on the high part of the cycle with some of them, similarly to Mode2 described previously, having effects at the transition from BR_h to BR_l as well. However, the support for modes 40 and above is almost exclusively located in the low quasi-steady state part of the cycle. Such segregation of the POD modes could have a negative impact on the reconstructed flow field as well as on a reduced order model resulting from truncation of the POD series as it would obliterate a significant part of the cycle.

Although Modes 1 and 2 are the most energetic, the complexity of the flow field generated at the transitions from one part of the cycle to the other prevents us from drawing definitive conclusions based only on the observation of these modes but provides a first order estimate of the impact of jet forcing on the temperature field, and particularly at the wall from a film cooling point of view. The 1st order effect of jet forcing on the wall temperature (corresponding to Mode1 in Fig. 13d-e, 14b and 15b) appears to be located directly around the jet exit and corresponds to the increase in spread observed in Fig. 4 at the jet onset as well as directly downstream of the jet exit due to increase in coolant mass flow. Since a_1 changes sign over the cycle (positive over the high part and negative over the low part), the first order effect of jet forcing is a decrease in wall temperature during the high part and an increase during the low part. Overall though, the highest values for Mode1 are located away from the wall suggesting a considerable waste of coolant in the free-stream. The second order effect represented by Mode2 shows that the transient regime (during which Mode2 is dominant) affects much more the wall temperature than the bulk effect of forcing. The effect of the jet onset (a_2<0) over the average temperature field appears to decrease the wall temperature locally around the jet exit due to local increase in spread, but increase it further downstream probably due to the increased entrainment associated with the starting structures lifting off of the wall. At the jet shutdown (a_2>0), the temperature around the jet increases due to the shrinking of the jet coverage associated with the decrease in coolant mass flow and the ingestion of cross-flow fluid. The downstream effect on the wall temperature is overall positive as the weaker vortical structures generated during the low part of the cycle do not entrain as much cross-flow and tend to remain attached to the wall.

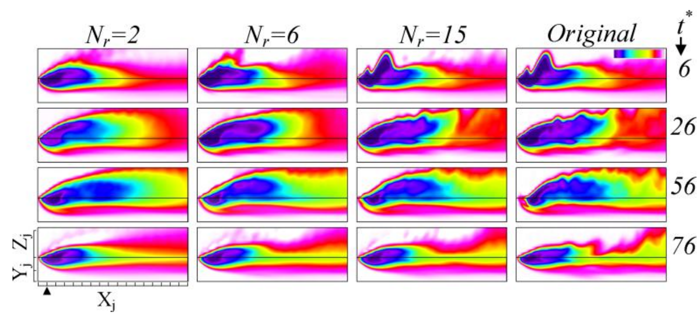

Figure 18 – Reconstructed temperature field for multiple values of N_r at 4 different phase locations.

For the sake of brevity, only the reconstructed temperature field will be presented in this document as the reconstructed velocity field requires tracing of streamlines to assess of the good reconstruction of all three velocity components, thus requiring a large amount of space to be appreciated. Figure 18 presents the reconstructed temperature fields with 2, 6, and 15 POD modes along with the original velocity field at four phase locked positions. Overall the temperature field appears relatively well reconstructed with only 15 POD modes. However, while the increase from 2 to 15 modes appears to bring significant improvement in the first 3 phase positions, the reconstruction at t*=76% does not show the same details as the one at t*=6% for N_r=15. This is an illustration of the effect of the absence of the higher order modes capturing the behavior in the quasi-steady low part of the cycle. It should be noted that the reconstructed temperature field at the wall does exhibit the dominant features of the original field with only 6 modes.

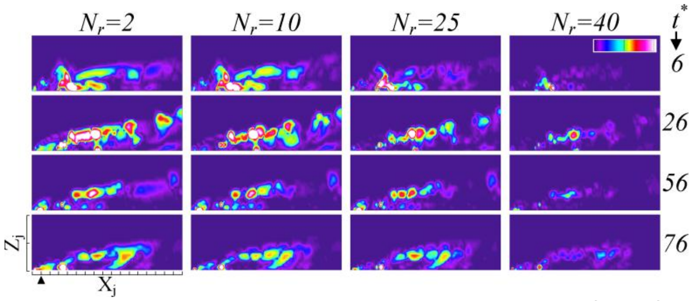

Figure 19 – Error on the reconstructed velocity field for different N_r values estimated with phase averaged fluctuation of kinetic energy. Maximum value (*white*) is 9%.

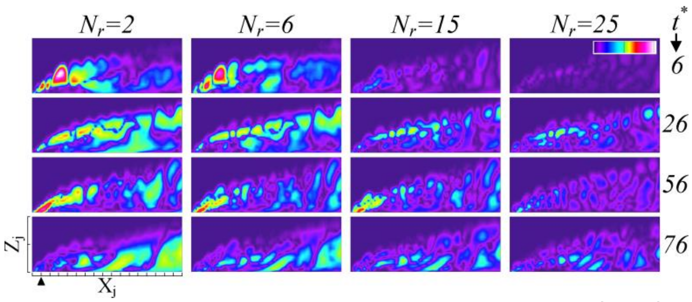

Figure 20 – Error on the reconstructed temperature field for different values of N_r estimated using the total value of the temperature. Maximum value (*white*) is 9%.

Although the reconstructed velocity field was not presented in the current document, an estimate of the error on the reconstruction is presented in Fig. 19. Since the POD analysis was performed on the phase averaged signal, it was impossible to base the estimate of the error on the turbulent kinetic energy. Instead, the error (e_r) was estimated on the kinetic energy of the phase average fluctuation normalized by the total kinetic energy such that if $\boldsymbol{U_r} = \overline{\overline{\boldsymbol{U}}} + \overline{\boldsymbol{U_r}}$ where $\boldsymbol{U_r}$ is the total reconstructed field, $\overline{\overline{\boldsymbol{U}}}$ is the time averaged signal (equal to the true time averaged field) and $\overline{\boldsymbol{U_r}}$ the reconstructed phase averaged fluctuation using N_r POD modes, then :

$$\boldsymbol{e_r} = \frac{\overline{\boldsymbol{U_r}}^2 + \overline{\boldsymbol{V_r}}^2 + \overline{\boldsymbol{W_r}}^2 - \overline{\boldsymbol{U}}^2 - \overline{\boldsymbol{V}}^2 - \overline{\boldsymbol{W}}^2}{\boldsymbol{U}^2 + \boldsymbol{V}^2 + \boldsymbol{W}^2} \quad (1)$$

Figure 19 shows that the error decreases consistently with increasing numbers of modes although not equally in time. Indeed while the error decreases significantly from N_r=2 to N_r=25 at t*=6%, it still stays relatively high for the other phase locations until N_r=40. The patch with high error at t*=26% corresponds to a zone where the velocity is relatively low thus any mismatch between the reconstructed and the true velocity field shows as high error. Even with N_r=40, the reconstructions at t*=26% and 76% still show some error due to the truncation although in absolute value below 4% of the total instantaneous kinetic energy.

As for the steady state, the error on the reconstructed temperature field was estimated as the relative error on total temperature (mean and fluctuation) and is presented in Fig. 20. Similarly to the velocity field, the error decreases consistently with increasing number of POD modes used in the reconstruction, although not across the phase positions. While the maximum error at t*=6% decreases from 9.2% at N_r=2 to 0.2% at N_r=25, corresponding to a factor of 46, it decreases at t*=26, 56 and 76% only by factors of respectively 2, 5, and 1.75. However, the relative error does not exceed a maximum of 4% across the cycle with N_r=10 and 2% with N_r=25 and above. On both velocity and temperature fields, it was verified that the error decayed to 0 when using all the modes for the reconstruction so that no loss of information was introduced by the proper orthogonal decomposition.

Simulation results from Case I at St=0.159 were analyzed using 3D-POD as well. Identical domain and spatial samplings were used. The temporal sampling consisted of 25 phase locked positions over 10 cycles accounting for a total of 250 snapshots. As for the previous forced case, the decomposition was carried out on both the complete time sequence and the phase averaged signal. The energy distribution and the phase diagrams for the first 6 pairs of modes are presented in Fig. 24. Once again, decompositions are identical up to the 10^{th} POD mode and diverge for higher order modes due to the presence of the turbulent fluctuation in the full time sequence series. As for the previous case at St=0.016, the decomposition on the phase averaged signal was preferred. The first noticeable difference between the two forced cases is found in the shape of the captured energy distribution. While in Fig. 12 at St=0.016 the energy distribution does not exhibit a particular shape, the one at St=0.159 assumes a clear stair-like shape. It should also be noted that the cumulative kinetic energy captured by the first two POD modes correspond to more than 65% of the total energy. Although in the presence of a forced case where the POD modes are automatically correlated to the forcing signal, the quasi-prefect circular distribution of the successive pairs of modes presented in the phase diagrams of Fig. 24b and 24c is a consequence of the stream-wise homogeneity of the flow making POD modes converge toward Fourier modes [12]. This result is a consequence of the fact that at St=0.159, multiple forcing cycles affect the flow field and that the dominant events are the generation and convection of the starting vortices. Hence the problem involves less length and time scales compared to the lower frequency case where the jet exhibited four distinct regimes each with distinct time and length scales.

POD modes issued from the decomposition of the velocity fields are presented in Fig. 21, 22 and 23. While the 0^{th} POD mode corresponds to the average flow field, the 1^{st} and 2^{nd} are virtually identical with the exception of a phase shift in the downstream direction as seen in the superposition of Q-criterion iso-surfaces in Fig. 21f. Both modes assume the shape

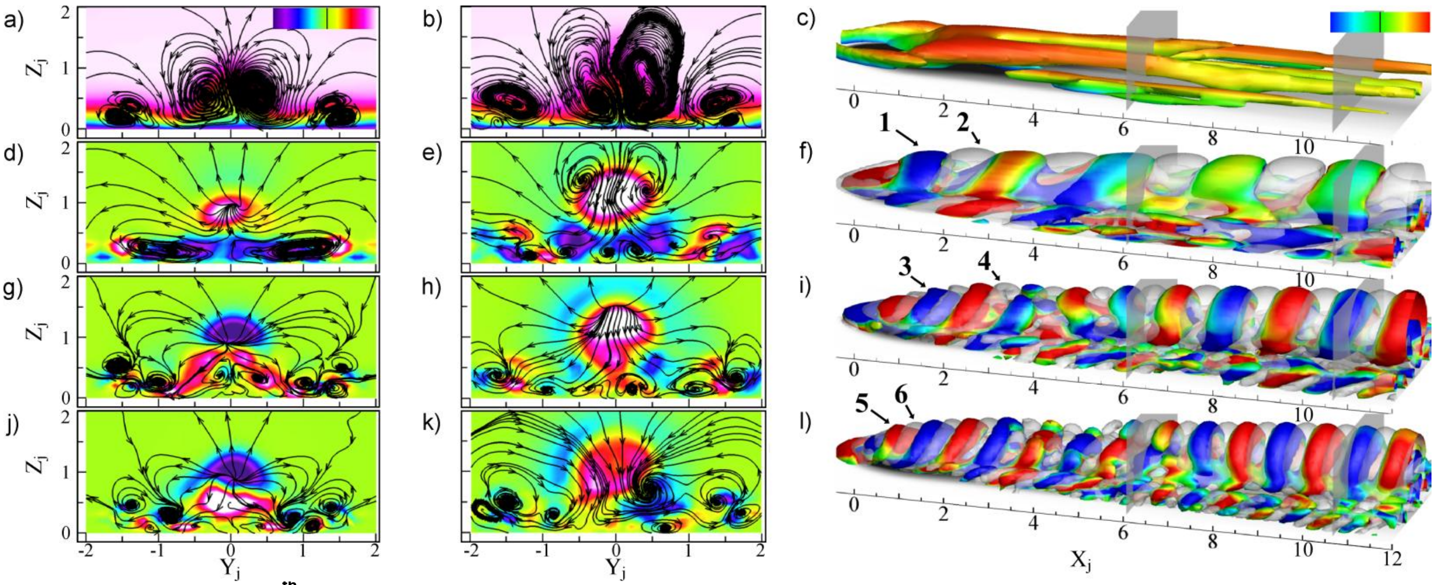

Figure 21 – Mean flow (0th POD Mode) and first significant velocity POD modes for Case I at St=0.159 a-d) Mode0; e-h) Mode1; i-l) Mode3; m-p) Mode5. Slices at X_j=6 (*left*), X_j=10.6 (*center*) with U-velocity contours and V-W streamlines. Q Criterion iso-surfaces (*right*) computed from corresponding POD modes and correlated mode (*white*) colored by the corresponding U-velocity and mean wall temperature contours (*grey scale*).

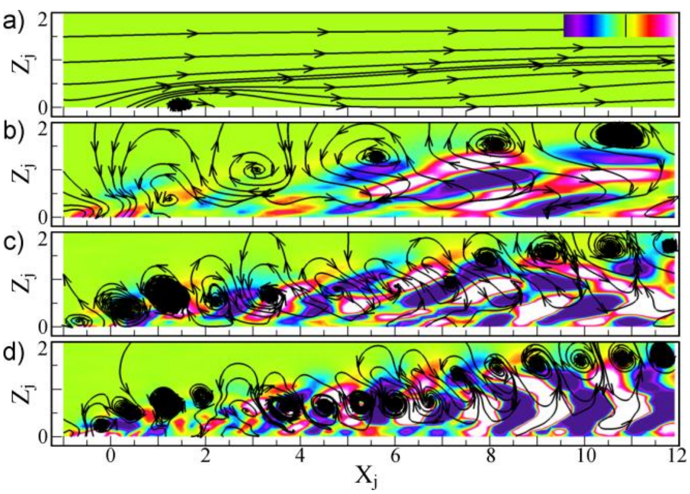

Figure 22 – Mean flow and first significant velocity POD modes for Case I at St=0.159 a-d) Mode0; e-h) Mode1; i-l) Mode3; m-p) Mode5. Slices at Y_j=0 with V-velocity contours and U-W streamlines.

of multiple large scale hairpin vortices penetrating deeply in the free stream. Along the hairpin vortices, a set of side vortices is also visible as well as in the X_j=6 cut of the flow field in Fig. 21d corresponding to the large scale side vortices formed near the wall close to the starting vortices and observed in instantaneous snapshots of Fig 7. The third and fourth modes, also largely identical with a shift in phase, constitute the first harmonic of the 1st and 2nd modes respectively. The phase diagram corresponding to these modes in Fig. 24b shows that while a_1 and a_2 complete a single revolution, a_3 and a_4 complete two. Similarly, Modes 5 and 6 are the second harmonics of Modes 1 and 2 respectively.

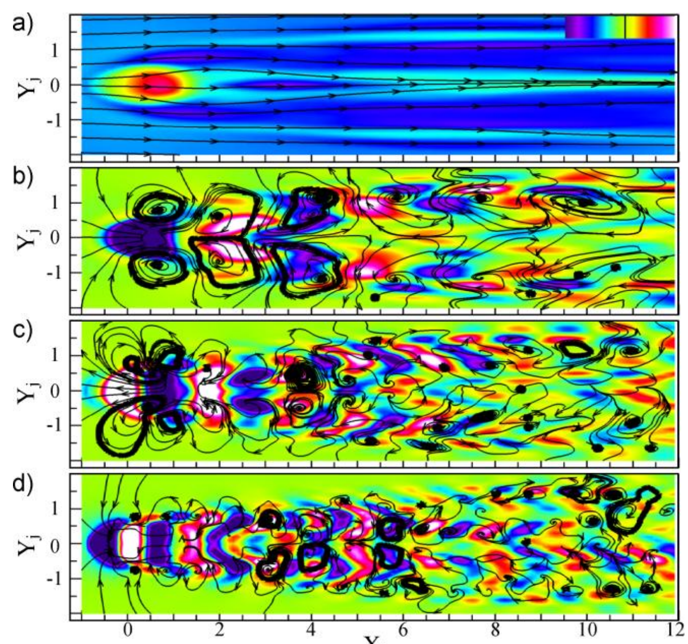

Figure 23 – Mean flow and first significant velocity POD modes for Case I at St=0.159 a-d) Mode0; e-h) Mode1; i-l) Mode3; m-p) Mode5. Slices at Z_j=0.25 with W-velocity contours and U-V streamlines.

As for the previous pulsed case, the modal coefficients a_1 through a_6 were plotted versus time along with the forcing signal in Fig. 16b. The phase shift between the correlated pairs of modes is easily quantifiable and corresponds to a quarter of the period for the first two, an eighth for modes 3 and 4 and a sixteenth for modes 5 and 6. Contrarily to the previous case, none of the modes appear to dominate over one particular part of the forcing cycle.

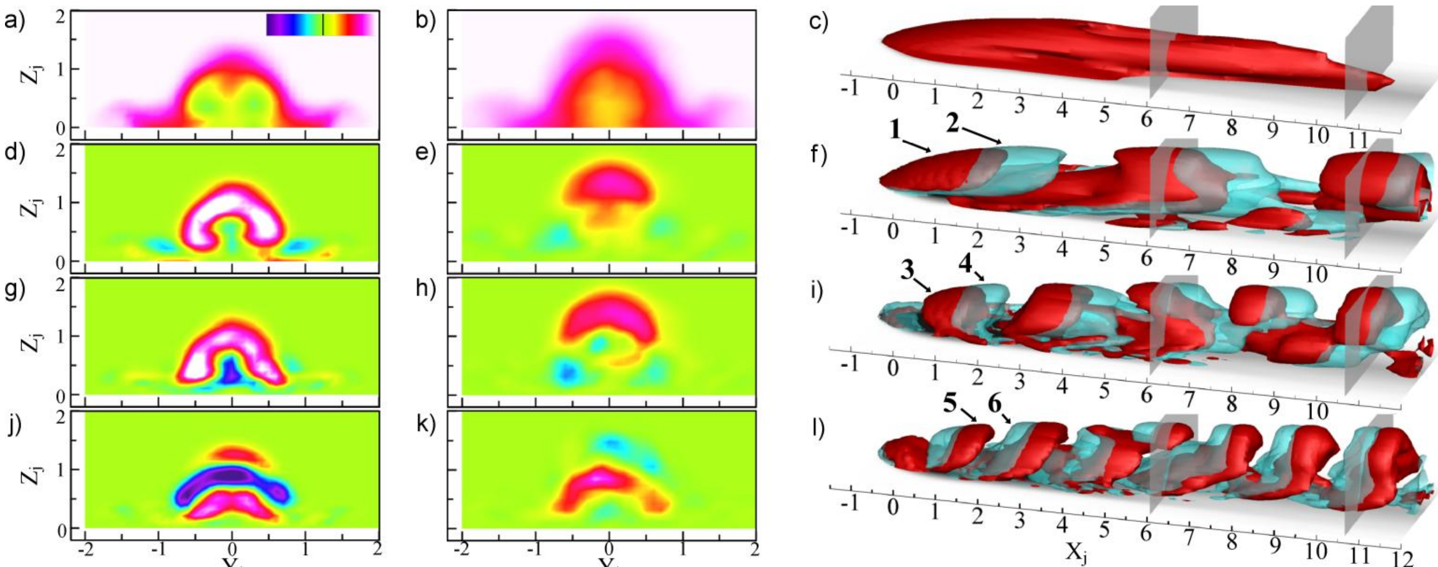

Figure 25 – Mean temperature field (0th POD mode) and first significant temperature POD modes for Case I at St=0.159 a-d) Mode0; e-h) Mode1; i-l) Mode3; m-p) Mode5. Slices at X_j=6 (*left*), X_j=10.6 (*center*) with temperature contours. Iso-T surfaces (*right*) computed from corresponding pairs of POD modes (*transparent*) and mean wall temperature contours (grey scale).

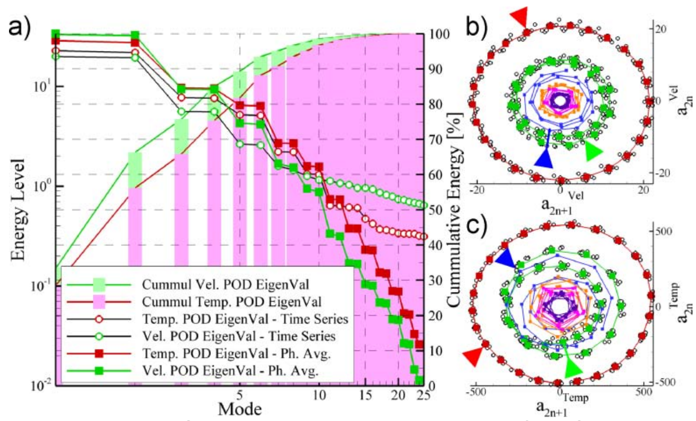

Figure 24 - POD decomposition metrics for Case I at St=0.159 from LES a) POD modes eigen values and cummulative energy for temperature and velocity; b) Velocity POD coefficients; c) Temperature POD coefficients. Open symbols correspond to full time sequence POD. Arrow points toward t*=0 in the time sequence.

The POD modes corresponding to the temperature field analysis are presented in Fig. 25, 26 and 27. As in the velocity POD, the first two modes are quasi-identical with a shift in the stream-wise direction. The iso-surfaces in Fig. 25f have a hairpin-like shape, alternating positive and negative values in the stream-wise direction as in the unforced case at BR=0.15. Higher order modes are paired similarly to the velocity field decomposition and constitute the successive harmonics of the first two modes. The evolution of the modal coefficients a_1 through a_6 with respect to time in Fig. 16b appears almost identical to the one obtained for the velocity field.

In opposition to the case at St=0.016, the impact of the different modes on the wall temperature decreases in scale and amplitude as mode order increases. Almost no impact on the wall temperature is observed beyond X_j=6. In the vicinity of the jet exit, the 1st temperature POD mode shows alternating positive and negative values due to the formation and convection of the starting structures. A band of high positive values covering part of the upstream edge of the jet exit is associated with the successive cross-flow ingestions and coverage increases occurring periodically at the jet shutdown and onset.

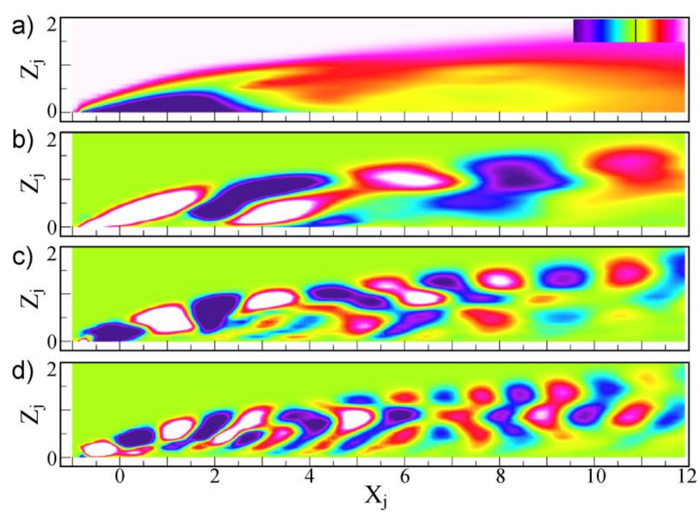

Figure 26 – Mean temperature field and first significant temperature POD modes for Case I at St=0.159 a-d) Mode0; e-h) Mode1; i-l) Mode3; m-p) Mode5. Slices at Y_j=0 with temperature contours.

The temperature field was reconstructed using 2, 4 and 6 POD modes as presented in Fig. 28. The reconstruction quality appears homogeneous with time and although the finest details are not represented, the fields including 4 and more modes

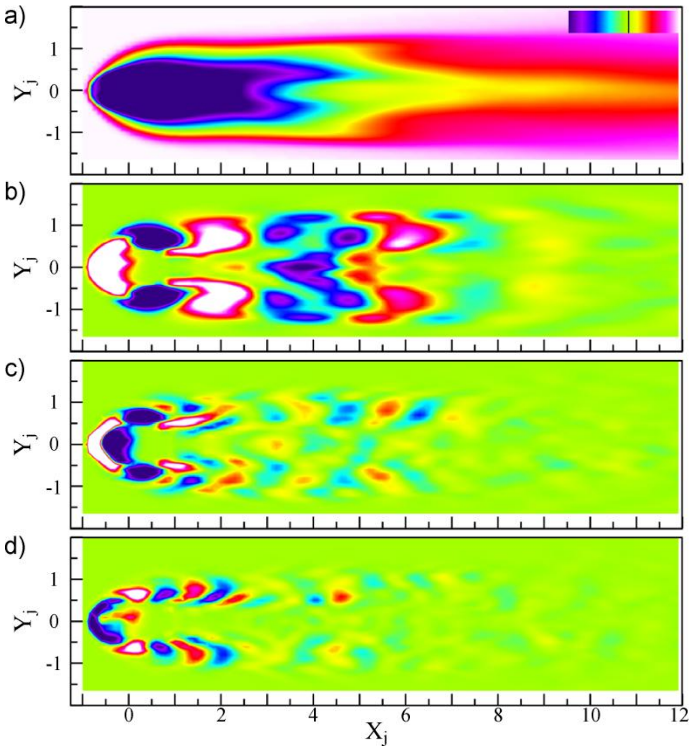

Figure 27 – Mean temperature field and first significant temperature POD modes for Case I at St=0.159 a-d) Mode0; e-h) Mode1; i-l) Mode3; m-p) Mode5. Slices at Z_j=0 with temperature contours.

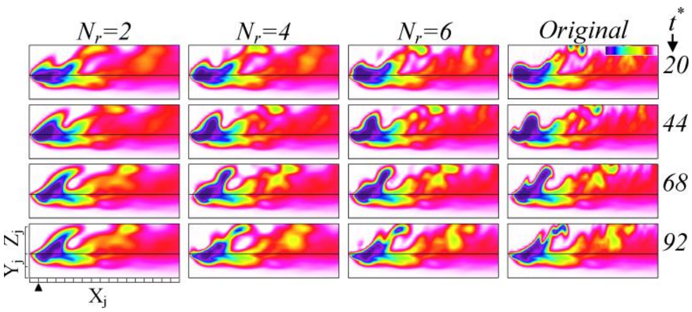

Figure 28 – Reconstructed temperature field for multiple values of N_r.at different phase location t*.

provide a reasonably good reconstruction. The error on the reconstructed velocity field and temperature fields were also investigated using different values of N_r. In Fig. 29 the error on the velocity field was estimated in the same way as for the lower forcing frequency case. The bulk of the error appears to reside in the region where the core of the starting vortex is located which also corresponds to the regions of higher velocity fluctuations. Conversely to the previous forced case the relative error decreases consistently with increasing number of included POD modes at all time steps. For N_r=15, the overall maximum error does not exceed 4%. Finally, the error on the temperature field was also computed and is presented in Fig. 30. As for the velocity reconstruction, the error decreases at all phase locations consistently with increasing number of POD modes included in the reconstruction. The effect of the individual modes is clearly visible on the reduction of the error as the scale of 'error patches' decreases with increasing values of N_r involving higher harmonics thus lower length scales. Six modes were required to obtain a maximum error less than 4% while 10 modes assured a maximum error on the temperature field of the order of 2%.

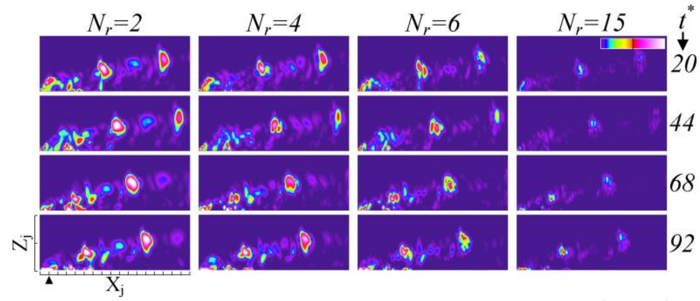

Figure 29 – Error on the reconstructed velocity field for different N_r values estimated using the phase averaged fluctuation of kinetic energy. Maximum value (*white*) is 6%.

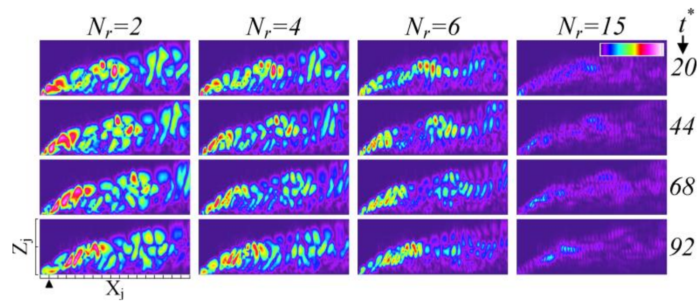

Figure 30 – Error on the reconstructed temperature field for different values of N_r estimated using the total value of the temperature. Maximum value (*white*) is 6%.

CONCLUSION

The pulsed film-cooling jet study presented here examined two different values for the high blowing ratio BR_h and two forcing frequencies. The qualitative experimental and numerical observations have revealed the formation of strong coherent vortical structures at the jet pulse onset in both cases, which introduced an increase in spread while also promoting mixing. At the jet pulse shutdown, cross-flow fluid ingestion at the jet exit and jet flow separation occurred, impacting the film cooling performance during the low part of the cycle for a significant period of time. Time averaged measurements of coverage and adiabatic effectiveness show that a pulsed jets can provide increased coverage over some of the comparable steady state counter-parts such as the one at constant pressure supply ($BR=BR_h$) but not over the one at constant mass flow ($BR=BR_m$). The phase averaged coverage and area averaged adiabatic effectiveness show that the transition from BR_h to BR_l is mainly to blame for the poor performance. Overall higher forcing frequencies led to poorer performance due to the domination of the transient features during the shorter cycles.

For the first time, 3D proper orthogonal decomposition was performed on a low blowing ratio pulsed jet at two distinct forcing frequencies. The analysis of the lowest frequency case (St=0.016) showed that the multiple POD modes have distinct support of action since several regimes are allowed to settle. Thus, due to the segregation of the POD modes, the truncation of the POD series in view of modeling the forced flow could lead to the suppression of the dynamics of part of the cycle. At the higher forcing frequency (St=0.159), the POD revealed the homogeneity of the flow in the stream-wise direction as the range of length and time scales introduced in the domain was limited.

Due to the significantly greater complexity of the problem at low forcing frequency, 40 POD modes were required to obtain less than 4% relative error on the velocity field, while the same error levels were reached with only 15 modes in the higher frequency case. The temperature field required fewer modes and respectively 10 and 6 modes were necessary at St=0.016 and St=0.159 to reach identical accuracy levels.

The POD analysis results presented here provide guidance towards satisfying the needs for the future development of reduced order models, while taking into account the fact that application of forcing requires a reduced order model that incorporates the effects of the forcing itself.

ACKNOWLEDGMENTS

The authors would like to thank the Air Force Office of Scientific Research for supporting this work under grants FA9550-06-1-0335 and FA9550-08-1-0440 as well as the Louisiana Board of Regents for supporting an instrumentation enhancement through grant LEQSF(2006-07)-ENH-TR-14.

REFERENCES

[1] Ligrani, P. M., Gong, R., Cuthrell, J. M., and Lee, J. S. "Bulk flow pulsations and film cooling--I. Injectant behavior," *International Journal of Heat and Mass Transfer* Vol. 39, No. 11, 1996, pp. 2271-2282.

[2] Womack, K. M., Volino, R. J., and Schultz, M. P. "Combined Effects of Wakes and Jet Pulsing on Film Cooling," *Journal of Turbomachinery* Vol. 130, No. 4, 2008, pp. 041010-12.

[3] Ou, S., Han, J.-C., Mehendale, A. B., and Lee, C. P. "Unsteady Wake Over a Linear Turbine Blade Cascade With Air and CO_2 Film Injection: Part I---Effect on Heat Transfer Coefficients," *Journal of Turbomachinery* Vol. 116, No. 4, 1994, pp. 721-729.

[4] Ekkad, S., Ou, S., and Rivir, R., B. "Effect of Jet Pulsation and Duty Cycle on Film Cooling From a Single Jet on a Leading Edge Model," *Journal of Turbomachinery* Vol. 128, No. July 2006, 2006, pp. 564-571.

[5] Coulthard, S. M., Volino, R. J., and Flack, K. A. "Effect of Jet Pulsing on Film Cooling-Part I: Effectiveness and Flow-Field Temperature Results," *Journal of Turbomachinery* Vol. 129, No. 2, 2007, pp. 232-246.

[6] Bidan, G., Vezier, C., and Niktopoulos, D. E. "Study of steady and modulated inclined film cooling jets using proper orthogonal decomposition – Part I: Unforced jets," *ASME TurboExpo*. Vancouver, Canada, 2011.

[7] Bidan, G., Oertling, J., Boulladoux, P. E., and Niktopoulos, D. E. "Experimental and numerical study of a steady and modulated transverse jets at low blowing ratios," *ASME TurboExpo*. Glasgow, Scottland, 2010.

[8] Nikitopoulos, D. E., Oertling, J., Acharya, S., and F, M. "On Active Control of Film-Cooling Flows," *ASME Turbo Expo: Power for Land, Sea and Air*. Barcelona, Spain, 2006.

[9] Ou, S., and Rivir, R., B. "Shaped-hole film cooling with pulsed secondary flow," *ASME Turbo Expo*. Barcelona, Spain, 2006.

[10] Johari, H., Pacheco-Tougas, M., and Hermanson, J. C. "Penetration and Mixing of Fully Modulated Turbulent Jets in Crossflow," *AIAA Journal* Vol. 37, No. 7, 1999, pp. 842-850.

[11] Vernet, R., Thomas, L., and David, L. "Analysis and reconstruction of a pulsed jet in crossflow by multi-plane snapshot POD," *Experiments in Fluids* Vol. 47, No. 4, 2009, pp. 707-720.

[12] Holmes, P., Lumley, J. L., and Berkooz, G. *Turbulence, Coherent Structures, Dynamical Systems and Symmetry*: Cambridge University Press, 1996.

